Digest Journal of Nanomaterials and Biostructures Vol. 15, No. 3, July-September 2020, p. 885 - 894

SYNTHESIS AND CHARACTERIZATION OF ZnO NANOPARTICLE FILMS ITS APPLICATION IN DYE-SENSITIZED SOLAR CELLS

S. KROBTHONG[a], S. NILPHAI[b], S. CHOOPUN[c], S. WONGRERKDEE[a,*]
[a]*Department of Physics, Faculty of Liberal Arts and Science, Kasetsart University Kamphaeng Saen Campus, Nakhon Pathom 73140, Thailand*
[b]*Physics Program, Department of Science and Technology, Faculty of Liberal Arts and Science, Roi Et Rajabhat University*
[c]*Department of Physics and Materials Science, Faculty of Science, Chiang Mai University, Chiangmai 50200, Thailand*

ZnO nanoparticle films were prepared using facile precipitation with low-toxic solvents. The nanoparticle films were observed in compact formation with uniform nanoparticle sizes, good distribution, and high specific surface areas. The chemical composition of Zn and O was detected and the optical band gap was estimated. The hexagonal wurtzite structure of ZnO nanoparticle films was confirmed by XRD and Raman. For dye-sensitized solar cell application, power conversion efficiency of 2.51% was measured due to the concurrent improvements of dye adsorption and charge collection efficiency. Therefore, ZnO nanoparticle films be considered as a well-functional material to turn suitable structures for DSSC application.

(Received May 23, 2020; Accepted September 2, 2020)

Keywords: ZnO, nanoparticles, Dye-sensitized solar cells, Dye adsorption, Charge collection efficiency

1. Introduction

Dye-sensitized solar cells (DSSCs) are interestingly investigated for over a decade due to its advantages including simple fabrication and low-cost technology requirements [1]. The major material used in DSSCs is wide-band gap semiconductors such as TiO_2, ZnO, SnO_2 which has major roles to support dye molecules and transfer excited electrons through external loads. For DSSC development, effective factors that affecting the photovoltaic (PV) performance should be improved such as dye adsorption, electron collection efficiency, harvesting efficiency, scattering effect [2]. An improvement of light-harvesting efficiency using β-$NaYF_4$:Yb^{3+}, Er^{3+} phosphors was reported to modify photoelectrodes as upconversion phosphors (UCPs)-TiO_2 composites [3]. The light-harvesting efficiency was improved due to the incorporation of UCPs because near-infrared (NIR) light region was absorbed. However, large recombination has occurred for the incorporation of UCPs. To solve the problem, the balance of UCPs and TiO_2 was performed to modify efficient UCPs-TiO_2 composite photoelectrodes for enhancing power conversion efficiency (PCE) of DSSCs. One of the interesting TiO_2 composites with graphene oxide (GO) based also studied [4]. A successful PV enhancement using TiO_2-reduced GO (rGO) heterojunction was demonstrated with the improved PCE of 5.36% in comparison to TiO_2 photoelectrode (3.94%). The enhancement has occurred due to concurrent improvement of electron transport and charge separation. Nevertheless, non-composite TiO_2 with nanostructures also has the potential to enhance the PV performance of DSSCs [5]. The TiO_2 was performed to a popcorn-like TiO_2 nanostructure and a high PCE of 7.56% was measured. The nanostructure was designed to coat over the larger size of commercial TiO_2 for creating scattering layers and it showed an increased incident photon-to-electron conversion efficiency (IPCE) which referring the light scattering improvement. Moreover, small sizes of the nanostructure also provided large surface areas for greater dye adsorption at the same time. According to the above literature, TiO_2-based materials are widely

* Corresponding author: sutthipoj.s@gmail.com

studied to fabricated as photoelectrodes because it has chemical stability and strong light absorption [6]. However, ZnO is an alternative candidate material replacing the TiO_2 due to specific property including high electron mobility, good charge carrier separation and collection, and non-toxicity [7,8]. The direct band gap of ZnO can better support the electrodynamic process of DSSCs in comparison to the indirect band gap of TiO_2. For the TiO_2-based DSSCs, the drawback of the electrodynamic process may occur including low use of solar spectrum, high recombination rate, and low electron transport property [8]. Moreover, it can be controllably synthesized to form nanostructures which are an important key for better optoelectronic device performance because nanostructures show many advantages such as chemical and thermal stability, high electrocatalytic ability, and high surface area [9]. Thus, ZnO nanostructures are considered for several devices including DSSCs [8]. It is well known that chemical synthesizing processes of ZnO nanoparticles required many solvents including toxic-solvents for controlling growth mechanisms to form nanoparticles. However, several toxic-solvents (i.g., ethanol, methanol, chloroform, n-butanol) harmful to humans and environments. Thus, distilled water with appropriate polymer assistance is considered for ZnO nanoparticle preparation in this work. The preparing process with low-toxic solvents could be considered as the friendly-environment process, but the high PCE may not be obtained for the non-toxic solvent process. Therefore, the balancing between the friendly-environment process and acceptable PCE is mentioned.

The ZnO nanoparticles were prepared using facile precipitation from starting materials of zinc acetate dihydrate and ammonium hydrogen carbonate at different molar ratios. The starting materials were separately dissolved in distilled water to form clear solutions. Then, the solutions were mixed under violent vibration. During the mixing process, a portion of the polymer was added to prevent aggregation or accumulation. The precursors carried ZnO nanoparticles were prepared on substrates to form ZnO nanoparticle films. The films were used as photoelectrodes for DSSC fabrication, and it was tested under standard measurement for evaluating the performance of the films for DSSC application.

2. Experimental

Zinc acetate dihydrate ($Zn(CH_3COO)_2{\cdot}2H2O$; ZAD) and ammonium hydrogen carbonate (NH_4HCO_3; AHC) were separately dissolved in distilled water under stirring and heating at 50 °C for 1 h to form the clear homogenous solutions. The concentration of AHC and ZAD solutions were comparatively prepared at AHC/ZAD molar ratios of 0.5, 1.0, and 1.5. The AHC solution was slightly dropped into the ZAD solution under stirring and heating. Then, a portion of polymer (polyethylene glycol 4000; PEG-4000) was added to reduce surfactant [10], and violent stirring was applied until the mixed solution form as viscous ZnO nanoparticle precursor. Next, the precursor was coated on fluorine-doped tin oxide (FTO) substrate using a screen-printing method and annealed at 550 °C for 1 h to form as ZnO nanoparticle films. To control the film's thickness, a thin polymer tap was used as a templating mask. For characterization, the films were investigated using various techniques including field emission scanning electron microscopy (FE-SEM), energy dispersive spectroscopy (EDS), X-ray diffractometry (XRD), Raman spectroscopy, Fourier-transform infrared spectroscopy (FTIR), and ultraviolet–visible (UV–Vis) spectroscopy.

For DSSC fabrication, ZnO nanoparticle films were moved to a Petri dish contained 0.3 mM N719 dye solution [1,7,11] for dye adsorption using the re-adsorption process as described in previous reports [12] to form as ZnO photoelectrodes. Finally, the photoelectrodes were used to fabricate DSSC devices [13,14]. Photovoltaic characteristics of DSSCs were examined using current density-voltage (J-V) measurement system, open-circuit voltage decay (OCVD), and electrochemical impedance spectroscopy (EIS).

3. Results and discussion

Morphological images of ZnO nanoparticle films explore the compact nanoparticle formation as shown in Fig. 1. ZnO nanoparticle films carried different sizes of nanoparticles for

the different AHC/ZAD molar ratios. The average particle sizes measured using free image-J software were 55.59±12.07, 68.48±14.07, and 118.44±28.11 nm for the ratios of 0.5, 1.0, and 1.5, respectively. It should be noted that particle sizes are insignificant differences between the ratios of 0.5 and 1.0. However, small particle sizes are appeared for the ratio of 0.5 because of the lack of OH^- anions for the chemical reaction at the low AHC concentration. The low OH^- anions could interact with Zn^{2+} cations with a slow rate which results in small particle size formation. On the other hand, larger particle sizes are found for the higher ratios of 1.0 and 1.5. It could suggest that aggregation may be occurred due to numerous OH^- ions. The particle size distribution of ZnO nanoparticles (Fig. 2) presents a comparative good distribution with similar sizes for the ratio of 1.0 which may be due to the cations-anions equilibrium. However, large particle sizes were formed for a higher ratio of 1.5. The effect may be described that excess OH^- anions repeating interact with the formed ZnO nanoparticles and aggregate at the ZnO surface which resulting in large particle size formation. For the surface-to-volume ratio analysis, specific surface areas (SSAs) were measured using the BET method. The measured SSAs were 35.75, 41.74, and 29.92 m^2/g for the ratios of 0.5, 1.0, and 1.5, respectively. Generally, it is well-known that high surface area will occur for small nanoparticle sizes. However, the ratio of 1.0 exhibits the highest SSAs even though it has higher particle sizes compared with the ratio of 0.5. The results, in this case, could explain due to the comparative well-uniform of nanoparticles for the ratio of 1.0. Moreover, it presents low aggregation with surrounding particles and low dense-deposited particles in comparison to other ratios.

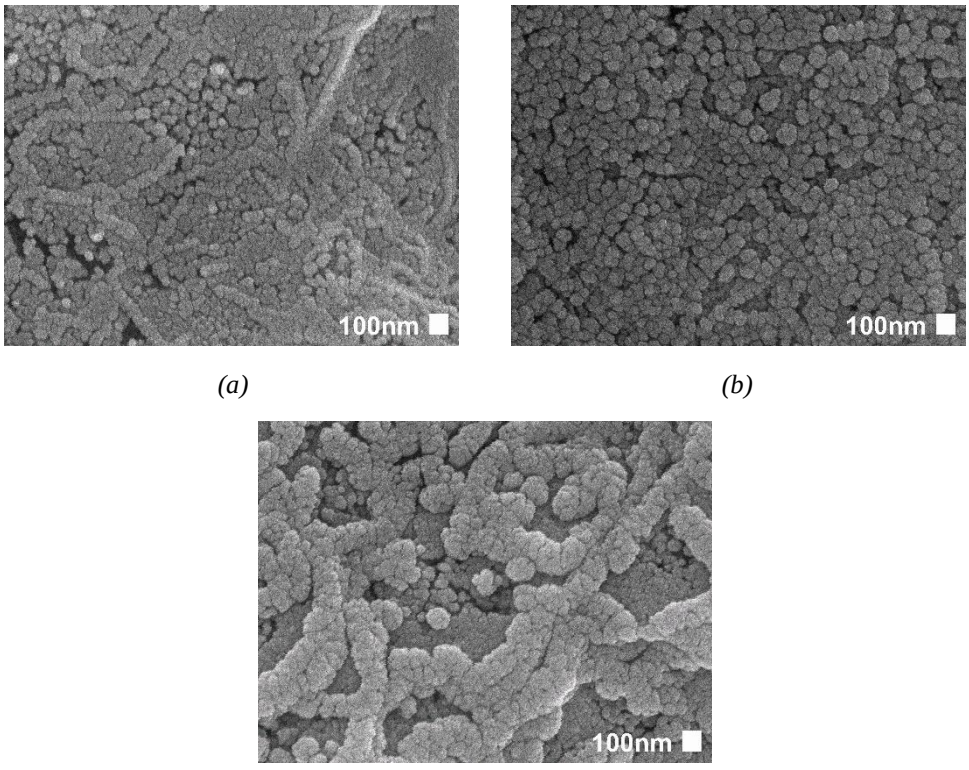

(a) *(b)*

(c)

Fig. 1 SEM images of ZnO nanoparticle films for AHC/ZAD molar ratios of (a) 0.5, (b) 1.0, and (c) 1.5.

According to the SEM images, some lacking particle zones are found for the ratios of 0.5 and 1.5. On the other hand, it is not observed for the ratio of 1.0. Thus, the equal molar ratio of starting materials could be considered an optimum condition for better compact ZnO nanoparticle films. Moreover, it can interpret that SSAs of ZnO nanoparticle films are not only governed by particle sizes but also caused by the forming quality of the films. Chemical compositions of ZnO

nanoparticle films were examined using EDS and similar atomic contents of Zn and O are approximated (Table 1). The results can determine that ZnO nanoparticle films are formed with low contamination for all conditions.

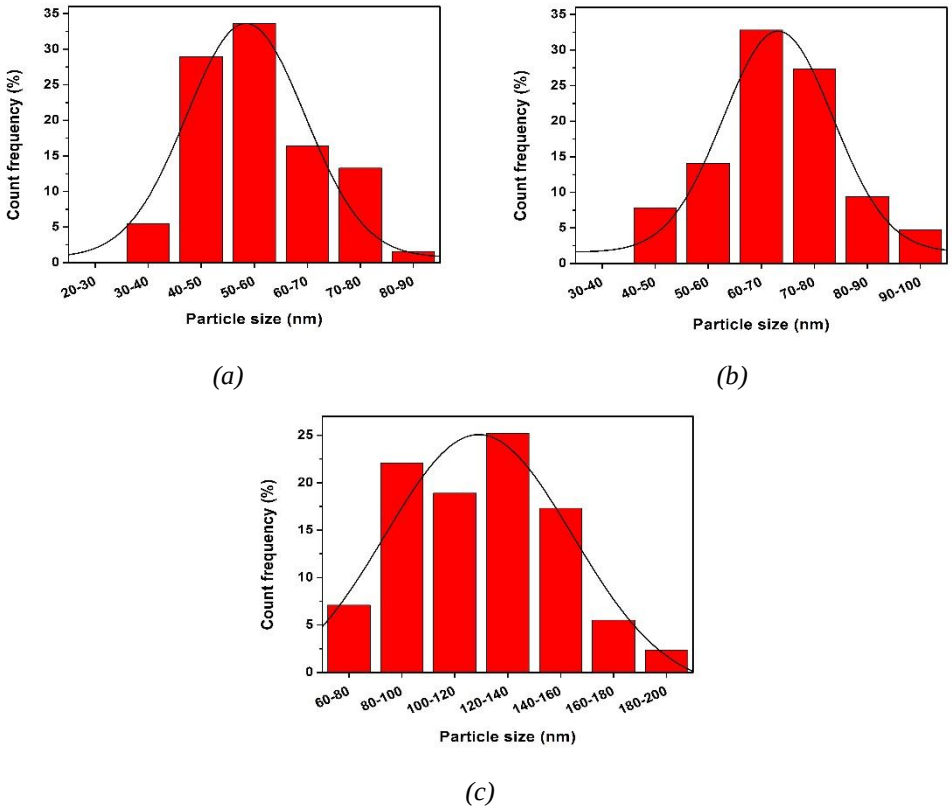

Fig. 2. Particle size distribution for AHC/ZAD molar ratios of (a) 0.5, (b) 1.0, and (c) 1.5.

Table 1. Chemical composition, optical band gap, and crystal parameter of ZnO nanoparticle films.

AHC/ZAD molar ratios	Atomic content (%)		E_g (eV)	D (nm)	a (Å)	c (Å)	c/a
	Zn	O					
0.5	56.75	43.25	3.21	18.230	3.248	5.208	1.603
1.0	53.67	46.33	3.22	20.411	3.249	5.209	1.603
1.5	55.33	44.67	3.23	18.348	3.252	5.211	1.603

Optical band gap energy (Eg) of ZnO nanoparticle films was estimated using the Tauc plot according to the Equation (1) [15,16].

$$(\alpha h\upsilon)^n = A\left(E_g - h\upsilon\right) \quad (1)$$

α and A are constant, h is the Plank's constant, υ is frequency, n is the index for material types which can be indexed as 1 and 2 for indirect band gap and direct band gap semiconductor, respectively. In this case, n = 2 for the direct band gap of ZnO nanoparticle films. From the plotting of $(\alpha h\upsilon)^2$ versus hυ as shown in Fig. 3, E_g can be estimated from the interception of linear fitting (can see in Table 1). The calculated E_g shows insignificant values implying the pure ZnO formation.

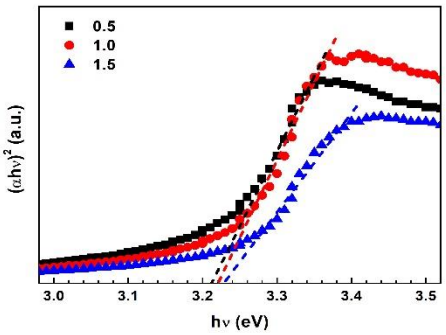

Fig. 3. The plot of $(\alpha h\upsilon)^2$ versus $h\upsilon$ of ZnO nanoparticle films for different AHC/ZAD molar ratios.

To characterize crystal structure, XRD and Raman were performed as shown in Fig. 4. The XRD diffraction peaks (Fig. 4(a)) for all conditions are well-corresponded to the hexagonal wurtzite (JCPDS no. 36-1451) [17], indicating the pure ZnO phase formation in the agreement to the EDS and E_g results. For crystal analysis, crystal size (D) was calculated from the 3 major peaks of (100), (002) and (101) planes using the Debye-Scherrer formula according to Equation (2) [16]. Also, the lattice constants "a" and "c" were calculated from Equation (3)-(4) [18] (can see in Table 1).

$$D = \frac{K\lambda}{\beta \cos\theta} \tag{2}$$

$$a = \frac{\lambda}{\sqrt{3}\sin\theta} \tag{3}$$

$$c = \frac{\lambda}{\sin\theta} \tag{4}$$

k is a constant (0.89), λ is the wavelength of X-ray (1.5406 Å), β is the full-width at the half-maximum (FWHM) intensity, θ is the diffraction angle. Crystal size exhibits the maximum value for the ratio of 1.0. The large crystal size implies high crystallinity with reduced defect formation. Also, the large crystal size could contribute to the long pathway for electron movement at the material surfaces before reaching grain boundaries. The long pathway is considered as the factor that could support active electrons for better charge transport in DSSC devices. Note that, c/a ratio shows the same value for all samples and closes to the JCPDS c/a ratio of 1.602 implying high crystallinity of the prepared ZnO nanoparticle films.

Raman shift in Fig. 4(b) confirms the hexagonal wurtzite structure of ZnO nanoparticle films in agreement with XRD results. The dominating peak at 438 cm^{-1} corresponded to the ZnO nonpolar optical phonons E_{2H} mode and the Raman active mode of the hexagonal wurtzite phase of ZnO [19-21] The peak at 331 cm^{-1} corresponded to the E_{2H}-E_{2L} mode due to the multi-phonon vibration. The peak at 387 cm^{-1} corresponded to the transverse optical modes of A_{1T}. Note that, disorder state or defect peak around 580 cm^{-1} is not observed indicating the pure ZnO formation [10,22].

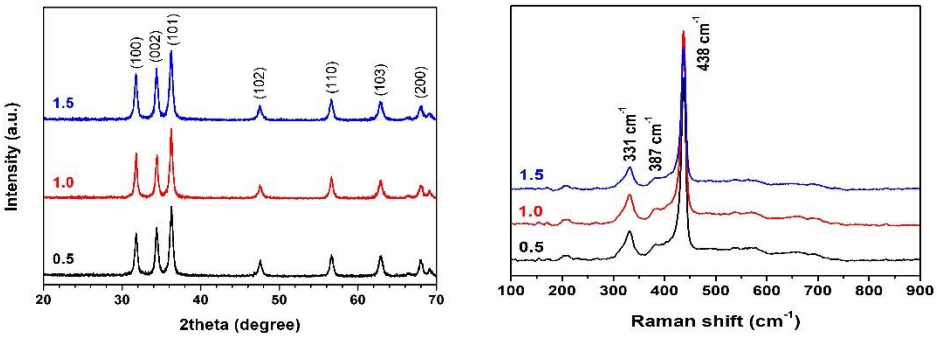

(a) *(b)*

Fig. 4. XRD patterns (a) and Raman shift (b) of ZnO nanoparticle films for different AHC/ZAD molar ratios.

For the DSSC application, all ZnO nanoparticle films were used as photoelectrodes to fabricate DSSC devices to evaluate the film's performance. Photovoltaic characteristics were measured under standard light illumination as shown in Fig. 5(a). Then, the photovoltaic parameters were calculated using Equation (5)-(6)[11], and listed in Table 2.

$$\mathrm{PCE} = \frac{J_{sc}V_{oc}FF}{P_{in}} \tag{5}$$

$$\mathrm{FF} = \frac{J_{max}V_{max}}{J_{sc}V_{oc}} \tag{6}$$

J_{sc} is the short-circuit current density, V_{oc} is the open-circuit voltage, FF is the fill factor, P_{in} is the incident illumination (100 mW/cm^2), J_{max} is the maximum current density, V_{max} is the maximum voltage. The maximum PCE is obtained for the ratio of 1.0. The ratio of 0.5 exhibits a small different PCE compared with the ratio of 1.0. On the other hand, the PCE is significantly decreased for a ratio of 1.5. It should be noted that low PCEs are obtained in this work compared with other reports [23,24]. However, the PCEs are in the several ranges of ZnO-based DSSCs. Thus, the ZnO nanoparticle films prepared by facile precipitation can be applied for DSSCs. Although the low PCEs are obtained, the use of low toxic solvents (distilled water) demonstrates the friendly-environment process which could be considered for further investigation.

To investigate the major parameter for PCE enhancement, dye adsorption was analyzed as shown in Fig. 5(b). The dye molecules adsorbed on ZnO nanoparticle films were extracted by immersing the films in NaOH solution. Then, absorbance spectra were measured and the amount of dye adsorption was calculated using the Beer-Lambert law [12].

$$A = c\varepsilon L \tag{7}$$

A is the absorbance, C is the dye concentration, ε is the molar extinction coefficient (ε=14,100 M^{-1} cm^{-1} at λ=515 nm), L is the path length of the measured dye solution. The dye molecules adsorbed on ZnO nanoparticle films are 6.28×10^{-9}, 6.49×10^{-9}, and 5.64×10^{-9} moles/cm^2 for the ratios of 0.5, 1.0, and 1.5, respectively. The dye adsorption explores a little different value for the ratios of 0.5 and 1.0. However, it decreases to the lowest value for the ratio of 1.5.

The relation between PCE and J_{sc} as the function of dye adsorption is observed as shown in Fig. 5(b). The PCE trend is the majoring correlation to the J_{sc} which be governed by dye adsorption. Thus, the improvement of PCE and J_{sc} is a direct correspondence to dye adsorption. Note that, it is believed that high dye adsorption could be supported by the high SSAs due to the better size distribution and good qualitative formation of ZnO nanoparticle films.

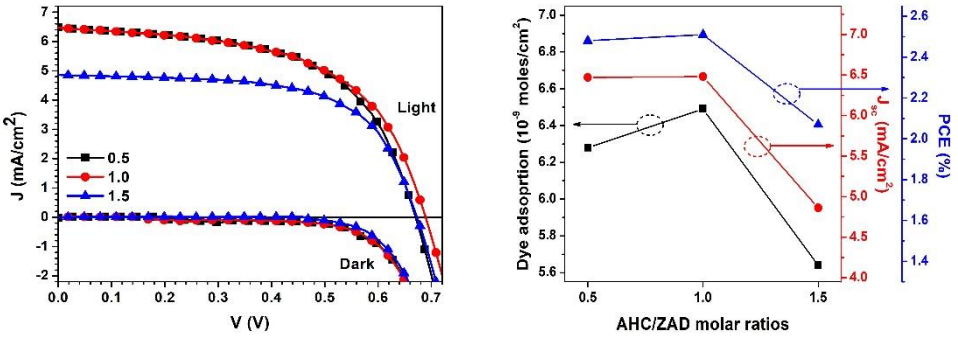

(a) *(b)*

Fig. 5. (a) J-V curves of DSSCs for different AHC/ZAD molar ratios, (b) correlation of dye adsorption, J_{sc}, and PCE.

Table 2. Photovoltaic parameters of DSSCs.

AHC/ZAD molar ratios	J_{sc} (mA/cm^2)	V_{oc} (V)	PCE (%)	FF
0.5	6.47 ± 0.02	0.67 ± 0.01	2.48 ± 0.02	0.58 ± 0.01
1.0	6.48 ± 0.01	0.69 ± 0.01	2.51 ± 0.01	0.56 ± 0.01
1.5	4.86 ± 0.02	0.67 ± 0.01	2.07 ± 0.03	0.64 ± 0.01

For charge dynamic behavior investigation, OCVD was measured as shown in Fig. 6(a) to estimate the recombination process in DSSCs. The measurement was performed by illuminating the simulated sunlight to DSSCs for exciting electrons in dye molecules and forming V_{oc}. After the illumination was turned off, the decay of V_{oc} for all DSSCs implying excited electrons recombine with holes for lowering energy to the ground state was detected. The ratio of 1.0 condition shows the slowest decrease in V_{oc}, indicating the lowest recombination rate. This effect could occur because large crystal sizes offer a long pathway for electron movement in the conduction band of ZnO nanoparticle films. The effect causes in long electron lifetime (τ) according to Fig. 6(b) which was analyzed from the Equation (8) [14,25].

$$\tau = -\frac{k_B T}{e}\left(\frac{dV_{oc}}{dt}\right)^{-1} \quad (8)$$

k_B is the Boltzmann constant, T is absolute temperature, e is the electron charge. Finally, charge collection efficiency (η_{cc}) of DSSCs was evaluated from charge transfer resistance (R_{ct}) using EIS measurement under a forwarding bias voltage of $-V_{oc}$ with and without illumination [10] as shown in Fig. 6(c,d). A brief description of EIS analysis, the EIS curves consist of two semicircles including small and large semicircles referring to the resistances of internal charge dynamics. The small semicircles are not observed for with and without illumination due to the obscuring of the larger semicircles. However, it is enough to calculate the η_{cc} using Equation (9) [26], as listed in Table 3.

$$\eta_{cc} = 1 - \frac{R_t}{R_{rec}} \quad (9)$$

R_t and R_{rec} are transport resistance and recombination resistance, respectively. The R_t and R_{rec} are

measured from the diameter of the large semi-circles with and without illumination, respectively. Generally, the high η_{cc} should give low R_t and high R_{rec} which reflecting fast electron transport and slow electron recombination, respectively [27]. The DSSCs fabricated with ZnO nanoparticle films for the ratio of 1.0 exhibit the highest η_{cc} compared with other DSSC devices. However, it is an insignificant different η_{cc} value between the ratios of 1.0 and 0.5. The high η_{cc} means excellent electron transport, leading to better DSSC performance. This behavior might be caused by concurrent improvements of high dye adsorption and large crystal size for increasing electron generation and electron lifetime, respectively. Therefore, the equal AHC/ZAD molar ratios could be an appropriate condition for ZnO nanoparticle film preparation with potential applications in DSSCs.

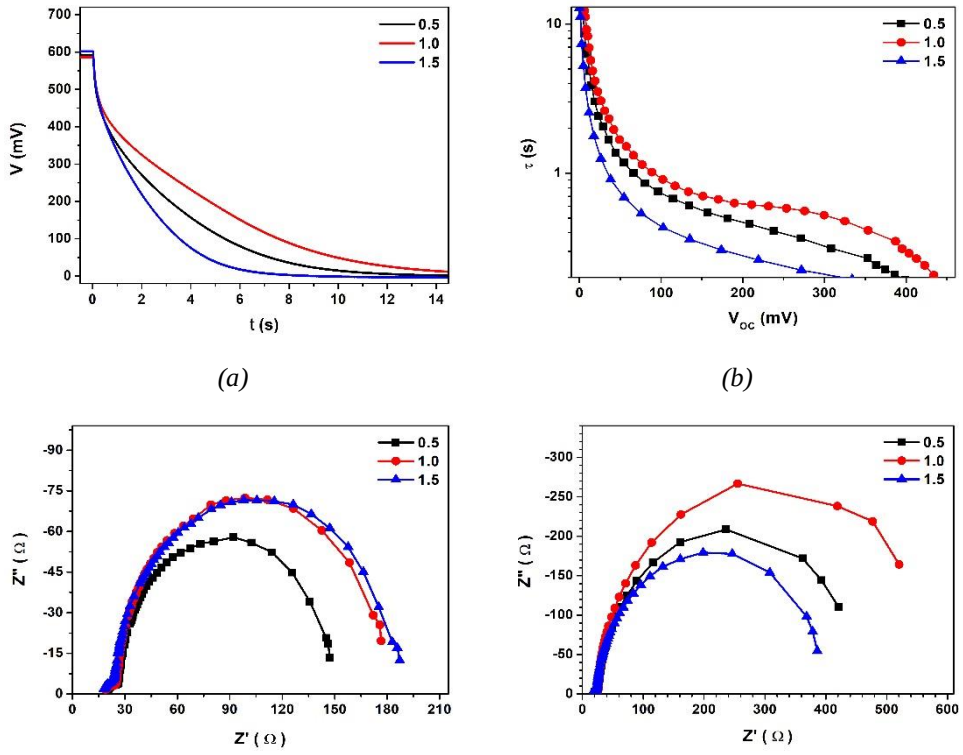

Fig. 6. Charge dynamic behaviors of DSSCs fabricated with ZnO nanoparticles films for different AHC/ZAD molar ratios; (a) OCVD, (b) electron lifetime, (c) EIS with illumination, (d) EIS without illumination.

Table 3. Charge recombination resistance, charge transport resistance, and charge collection. efficiency.

AHC/ZAD molar ratios	R_{rec} (Ω)	R_{ct} (Ω)	η_{cc}
0.5	461.4	134.7	0.77
1.0	590.6	165.9	0.78
1.5	403.4	172.5	0.70

4. Conclusions

ZnO nanoparticle films were prepared using facile precipitation from zinc acetate dihydrate and ammonium hydrogen carbonate under violent vibration with polymer assistance for avoiding toxic solvents. The viscous ZnO nanoparticle precursors were coated on FTO substrates and annealed to form ZnO nanoparticle films. Compact nanoparticle films were observed with high specific surface areas. Chemical composition of Zn and O was detected referring to the pure ZnO formation. Hexagonal wurtzite structure with high crystallinity of ZnO nanoparticle films was confirmed by XRD and Raman. DSSCs fabricated with ZnO nanoparticle films showed an enhanced average PCE of 2.51%.

The PCE enhancement is due to the concurrent improvements of dye adsorption and charge collection efficiency. The high dye adsorption is caused by high specific surface areas of ZnO nanoparticle films with uniform particle sizes and good nanoparticle distribution. The charge collection efficiency is improved by large crystal sizes which providing the long pathway for better electron transport with low recombination. Therefore, ZnO nanoparticle films prepared using facile precipitation with low-toxic solvent under the appropriate condition could be considered as a well functional material to turn suitable structures for DSSC application with the friendly-environment process.

Acknowledgments

This work was supported by the Faculty of Liberal Arts and Science, Kasetsart University Kamphaeng Saen Campus. Authors would like to acknowledge the Applied Physics Research Laboratory (APRL), Department of Physics and Materials Science, Faculty of Science, Chiang Mai University for facility supports.

References

[1] V. Rondán-Gómez, I. Montoya De Los Santos, D. Seuret-Jiménez, F. Ayala-Mató, A. Zamudio-Lara, T. Robles-Bonilla, M. Courel, Applied Physics A **125**, 836 (2019).
[2] N. A. Karim, U. Mehmood, H. F. Zahid, T. Asif, Solar Energy **185**, 165 (2019).
[3] X. Mao, J. Yu, J. Xu, L. Wan, Y. Yang, H. Lin, J. Xu, R. Zhou, Physica Status Solidi A **216**, 1900382 (2019).
[4] X. Y. Gu, E. Z. Chen, M. Y. Ma, Z. Y. Yang, J. L. Bai, L. L. Chen, G. Z. Sun, Z. X. Zhang, X. J. Pan, J. Y. Zhou, E. Q. Xie, Journal of Physics D **52**, 095502 (2019).
[5] Y.-Z. Chen, R.-J. Wu, L.-Y. Lin, W.-C. Chang, Journal of Power Sources **413**, 384 (2019).
[6] Q. Liu, J. Wang, Solar Energy **184**, 454 (2019).
[7] V. Consonni, J. Briscoe, E. Kärber, X. Li, T. Cossuet, Nanotechnology **30**, 362001 (2019).
[8] J. Theerthagiri, S. Salla, R. A. Senthil, P. Nithyadharseni, A. Madankumar, P. Arunachalam, T. Maiyalagan, H.-S. Kim, Nanotechnology **30**, 392001 (2019).
[9] M. Z. H. Khan, X. Liu, Journal of Electronic Materials **48**, 4148 (2019).
[10] S. Wongrerkdee, S. Moungsrijun, S. Sujinnapram, S. Krobthong, S. Choopun, Bulletin of Materials Science **42**, 91 (2019).
[11] J. M. Cole, G. Pepe, O. K. Al Bahri, C. B. Cooper, Chemecal Reviews **119**, 7279 (2019).
[12] S. Sutthana, D. Wongratanaphisan, A. Gardchareon, S. Phadungdhitidhada, P. Ruankham, S. Choopun, Journal of Nanomaterials **2016**, 7403019 (2016).

[13] S. Sutthana, D. Wongratanaphisan, A. Gardchareon, S. Phadungdhitidhada, P. Ruankham, S. Choopun, Surface and Coatings Technology **306**, 30 (2016).
[14] S. Moungsrijun, S. Sujinnapram, S. Choopun, S. Sutthana, Monatshefte für Chemie **148**, 1191 (2017).
[15] R.P. Chauhan, D. Gehlawat, A. Kaur, Journal of Experimental Nanoscience **9**, 871 (2014).
[16] S. Moungsrijun, S. Sujinnapram, S. Sutthana, Monatshefte für Chemie **148**, 1177 (2017).
[17] G. Malik, S. Mourya, J. Jaiswal, R. Chandra, Materials Science in Semiconductor Processing **100**, 200 (2019).
[18] S. Patra, D. Verma, A.K. Kole, C.S. Tiwary, D. Kundu, S. Chaudhuri, P. Kumbhakar, Materials Today Communications **12**, 133 (2017).
[19] A.-I. Istrate, F. Nastase, I. Mihalache, F. Comanescu, R. Gavrila, O. Tutunaru, C. Romanitan, V. Tucureanu, M. Nedelcu, R. Müller, Journal of Sol-Gel Science and Technology **92**, 585 (2019).
[20] T. D. Malevu, B. S. Mwankemwa, M. A. M. Ahmed, T. E. Motaung, K. G. Tshabalala, R. O. Ocaya, Journal of Electronic Materials **48**, 6954 (2019).
[21] A. Báez-Rodríguez, L. Zamora-Peredo, M. G. Soriano-Rosales, J. Hernández-Torres, L. García-González, R. M. Calderón-Olvera, M. García-Hipólito, J. Guzmán-Mendoza, C. Falcony, Journal of Luminescence **218**, 116830 (2020).
[22] K. L. Chiu, S. Shang, Y. Wang, S. Jiang, Ceramics International **46**, 2002 (2020).
[23] J. A. Anta, E. Guillén, R. Tena-Zaera, The Journal of Physical Chemistry C **116**, 11413 (2012).
[24] Q. Zhang, C. S. Dandeneau, X. Zhou, C. Cao, Advanced Materials **21**, 4087 (2019).
[25] P. Ruankham, D. Wongratanaphisan, A. Gardchareon, S. Phadungdhitidhada, S. Choopun, T. Sagawa, Applied Surface Science **410**, 393 (2017).
[26] Y. Dou, F. Wu, C. Mao, L. Fang, S. Guo, M. Zhou, Journal of Alloys and Compounds **633**, 408 (2015).
[27] S. N. F. Zainudin, H. Abdullah, M. Markom, Journal of Materials Science: Materials in Electronics **30**, 5342 (2019).